5.1 Introduction

In comparison with other precious noble metals, copper nanoparticles (CuNPs) as catalysts are much cheaper. They have shown excellent catalytic activities in various reactions [Deka *et al*. (2014), Karakhanov *et al*. (2010)]. Recent review summarizes different catalytic applications of Cu and Cu based nanomaterials [Gawande *et al*. (2016)]. The chemical reduction route is a convenient method for the synthesis of copper nanoparticles. In this technique the nanoparticle characteristics can be controlled by varying the different experimental parameters like concentrations, redox potentials, temperature, and pH [Singh *et al*. (2009), Goia (2004), Sergeev (2001)].

However, CuNPs under ambient conditions are susceptible to surface oxidation since Cu oxide phases are thermodynamically more stable than pure Cu [Chang *et al*. (2013)]. There are some reports for the synthesis of CuNPs where green reducing agents are used. An attempt to reduce copper salt solution using extract of Euphorbia esula L leaves has been reported. Though, some reduced Cu was formed; the product also showed the presence of CuO and Cu_2O phases. Thus, the reduction was not complete in presence of weak reducing agent [Nasrollahzadeh *et al*. (2014)]. There is one more report for the synthesis of CuNPs in presence of glucose as reducing agent where the reduction of copper salt was achieved via formation of Cu_2O intermediate [Blosi *et al.* (2014)]. They reported that using weak reducing agent, the ratio between metal salt to reducing agent should be very high and microwave irradiation of 40 min is required at high temperature. Therefore, the synthesis of CuNPs has usually been attempted using strong reducing agents and inert atmosphere in non-aqueous media to prevent or minimize surface oxidation.

In contrast to this, the synthesis of CuNPs is possible in alkaline pH conditions even in aqueous medium when hydrazine hydrate (HH) is used as the reductant. Such a synthesis

does not require inert gas atmosphere due to in situ generation of N_2 [Deng *et al*. (2013), Singh *et al*. (2010), Wu and Chen (2004)]. The reductant used was in excess in these investigations. The present investigation, therefore, employs alkaline hydrazine hydrate (AHH) as reductant for aqueous phase preparation of CuNPs in presence of polyvinyl pyrrolidone (PVP) as the stabilizer. This enables better control of over different stages of CuNPs synthesis. Furthermore, variation in the amount of AHH enables the delineation of different stages of growth of CuNPs.

There are a few studies available on Nip reduction over CuNPs as the catalyst with little or no kinetic studies. Accordingly, Deka *et al.* (2014) reported the catalytic activity of in situ generated CuNPs (without using any stabilizer) for reduction of Nip to AP at room temperature. Similarly, Prucek *et al.* (2009) investigated polyacrylic acid (PAA) stabilized CuNPs catalyzed reduction of Nip to AP. In both cases the presence of Cu_2O in CuNPs samples was noted by these authors [Deka *et al.* (2014), Prucek *et al*. (2009)]. Further, Santhanalakshmi *et al.* (2012) synthesized CuNPs with HH in presence of three different stabilizers. The effect of different stabilizers on catalytic Nip reduction was also reported. Recently, Kaur *et al.* (2014) have also reported polyacrylic acid (PAA) stabilized CuNPs (without any Cu_2O formation) catalysed Nip reduction to AP. Tan *et al.* (2015) reported the effect of chitosan on synthesis and catalytic activity of CuNPs and reported 2 : 1 chitosan to Cu salt ratio has higher catalytic activity compared to other ratios.

CuNPs also exhibit visible range LSPR absorbance. Therefore, it can also act as plasmonic catalyst in photocatalytic studies. However, in comparison to Au and Ag, the LSPR of CuNPs is the least [Bansal *et al.* (2014)]. There are reports on this effect of CuNPs in presence of inert support or carbon based materials. Graphene-supported CuNPs by reducing Cu_2O/graphene composites was synthesized in a mixture of H_2 and Ar at 500 ^{0}C

[Guo *et al.* (2014)]. These nanoparticles were then used as plasmonic photocatalysts for the selective synthesis of aromatic azo compounds from their corresponding nitro compounds under visible light irradiation. The dependency of coupling reaction on intensity and the wavelength of the incident light suggests the reaction is photodriven process. Most probably, the localized SPR effect of CuNPs excites the energetic electrons on its surface to facilitate the N−O bond cleavage in the aromatic nitro compounds, leading to the formation of corresponding azo compounds. In another example, Cu/SiO_2-catalyzed selective propylene epoxidation was improved by visible light irradiation [Marimuthu *et al.* (2013)]. The visible light irradiation causes a sharp increase in the selectivity for propylene epoxide from ~20 % to ~50 % in presence of Cu/SiO_2 NPs due to localized SPR produced on the NPs.

This Chapter first describes the aqueous phase synthesis of two different sizes of PVP stabilized pure CuNPs. Then, different aspects of catalytic properties of these CuNPs samples are investigated by using them as catalysts for: *p*-nitrophenol (Nip) reduction by (i) sodium borohydride ($NaBH_4$), ii) glycerol (Gly). The catalytic activity of these CuNPs for Fenton like oxidative degradation of methyl orange (MO) was also investigated. The effect of temperature on the reaction and thereby on activation energies is discussed. Finally, the effect of visible light irradiation on the catalytic activities of these CuNPs is also studied.

5.2. Experimental details

5.2.1 Synthesis of CuNPs stabilized by PVP

Materials used for the synthesis of CuNPs were $Cu(NO_3)_2.3H_2O$ (Merck), polyvinylpyrrolidone (PVP) (Himedia), NaOH (Merck), and hydrazine hydrate (Merck). All reagents used were of analytical reagent grade and were used without further

purification. Equal volumes of 0.0025 M NaOH and 0.05 M hydrazine hydrate were mixed to prepare the alkaline hydrazine hydrate (AHH) solution (with pH = 9). The copper salt solution was prepared by adding 10 wt % PVP to 5 mL aqueous solution of 0.01 M $Cu(NO_3)_2.3H_2O$. The AHH solution was now added in a drop wise manner to the copper salt solution with continuous stirring. The final reaction is $2Cu^{2+} + N_2H_4 + 4OH^- \rightarrow 2Cu + N_2 + 4H_2O$ [Grouchko *et al.* (2009), Wu and Chen (2004)]. As the amount of AHH added was increased, the initially blue colored copper salt solution changed first to yellow, then orange, and finally to a reddish-brown color with precipitate formation. Based on this understanding, two samples B1 and B2 corresponding to stable orange and reddish brown stages, were prepared. The samples B1 and B2 CuNPs is prepared by adding 5 mmol and 16 mmol AHH respectively to precursor salt solution with stabilizer [$(Cu(NO_3)_2.3H_2O$ and 10 wt % PVP as mentioned above]. The reaction vessel was then closed immediately after AHH addition. Figure 5.1 shows the as prepared B1 (orange) and B2 (reddish-brown) CuNPs sol samples. In general, the prepared samples were found to be stable for at least 4 weeks in closed conditions.
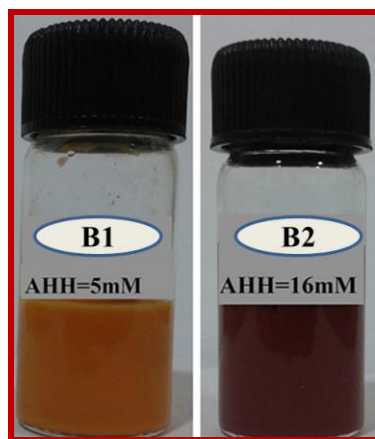
Figure 5.1 Freshly prepared orange (B1) and reddish-brown (B2) CuNPs sols.

5.2.2 Catalytic reduction and oxidation

5.2.2.1 Catalytic Nip reduction with NaBH$_4$

The experimental details for the Nip reduction with NaBH$_4$ in presence of B1 and B2 CuNPs are identical to the protocol described in sub-section 3.2.2.1 of Chapter-3.

5.2.2.2 Catalytic Nip reduction with glycerol

The particulars of experiments for Nip reduction with Gly as reductant in presence of B1 and B2 CuNPs as catalyst is identical to the protocol described in sub-section 3.2.2.2 of Chapter-3. The temperature at which this reaction was carried out is 306 K.

5.2.2.3 Catalytic oxidation of MO dye

The experimental detail for oxidative MO degradation with H$_2$O$_2$ in presence of B1 and B2 CuNPs is identical to the protocol described in sub-section 3.2.2.3 of Chapter-3.

5.2.3 Effect of exposure to visible light

Photocatalytic activity is measured by placing the reaction mixtures in photocatalytic chamber as described in Chapter-2. The temperature of the photocatalytic chamber was measured to be 306 K.

5.2.3.1 Photocatalytic enhancement of Nip reduction with glycerol

The reaction mixture with catalyst (B1 and B2 CuNPs) was prepared similar to the protocol given in section 3.2.2.2. This was then irradiated by visible light from cool white LED source (approximately 940 watts/m^2) in the photocatalytic chamber at 306 K. The absorption spectrum of the reaction mixture was recorded after every 10 minutes time interval.

5.2.3.2 Photocatalytic oxidation of methyl orange dye

The reaction mixture with the catalyst was prepared as given in section 3.2.2.3. The reaction mixture was kept in the photocatalytic chamber at 306 K and then irradiated by visible light from cool white LED source (approximately 940 watts/m^2). The kinetics and photocatalytic activities were measured for both B1 and B2 CuNPs catalyst samples in this manner.

5.3. Results and discussion

5.3.1 Characterization of CuNPs stabilized by PVP

To understand interactions between CuNPs and the polymeric stabilizer, the FT-IR spectra of PVP and PVP stabilized CuNPs were compared (Figure 5.2). The peak at 1660 cm^{-1} (PVP FT-IR) corresponds to the C = O vibrational mode.
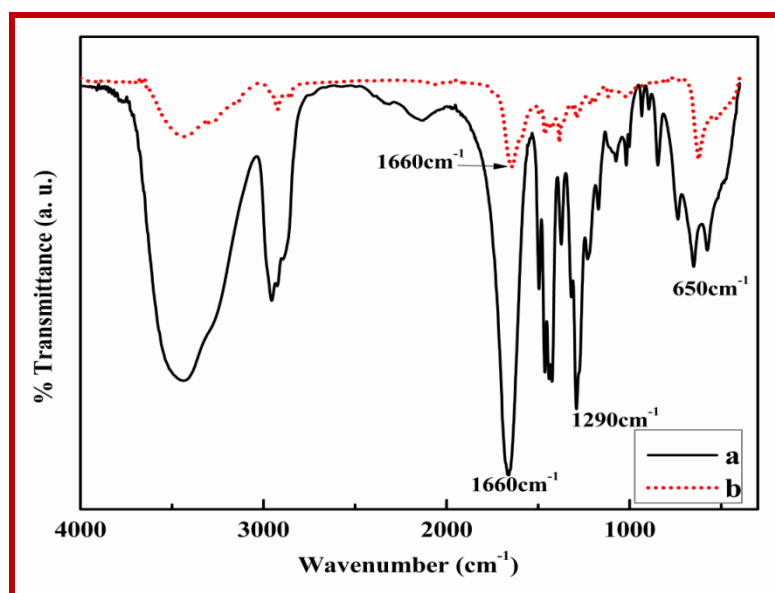
**Figure 5.2** FT-IR spectra of pure PVP (a) and B2 CuNPs stabilized by PVP (b).

On the contrary, the FT-IR spectrum of PVP stabilized CuNPs displayed a weak red-shifted C = O peak at 1640 cm^{-1} [Xian *et al*. (2012)]. A sharp band at 1290 cm^{-1} shown by PVP FT-IR was found to be much weakened in Cu-PVP spectrum, indicating the change in dipole moment of C-N bond. Furthermore, the peak at 650 cm^{-1} in PVP is shifted to 620 cm^{-1} in the Cu-PVP spectrum due to the Cu interaction with C-N bond. From this analysis, it appears that PVP chemisorbs on to the CuNPs surface using its carbonyl oxygen and the ring nitrogen affecting the surface electron density. It can also affect the LSPR properties of these nanoparticles.
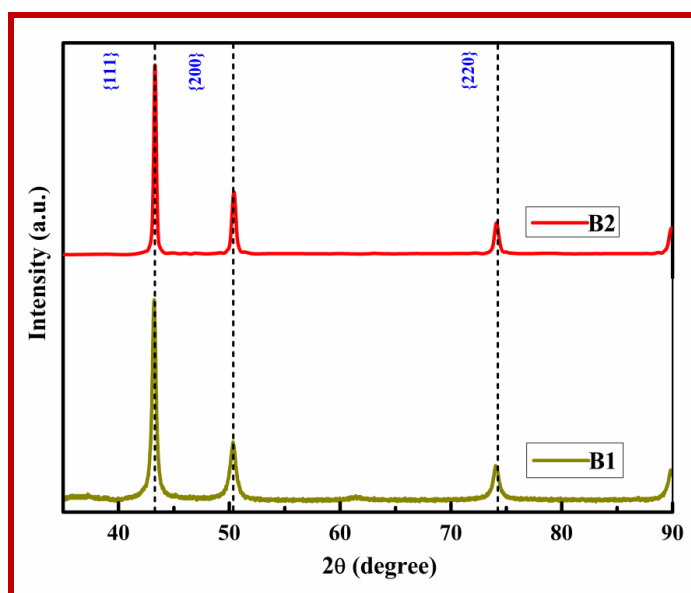
Figure 5.3 X-ray powder diffraction patterns of B1 and B2 CuNPs samples.

The X-ray diffraction pattern of the powdered B1 and B2 CuNPs samples are shown in Figure 5.3. As per the data reported for FCC copper in JCPDS ICDD (card no. 87-0720), three peaks were observed at 2θ values 43.31^{o}, 50.43^{o} and 74.13^{o} corresponding to {111}, {200} and {220} reflections respectively.

The TEM micrographs of the prepared CuNPs samples and the corresponding electron diffraction patterns are shown in Figure 5.4. The average size of CuNPs in sample B1 is found to be ~11 nm from its TEM images (Figure 5.4 (a)). Here the nanoparticles appear to be embedded in some kind of PVP polymer matrix. On addition of more AHH, the CuNPs (Sample B2) average size further decreases to ~9 nm (Figure 5.4 (c)).
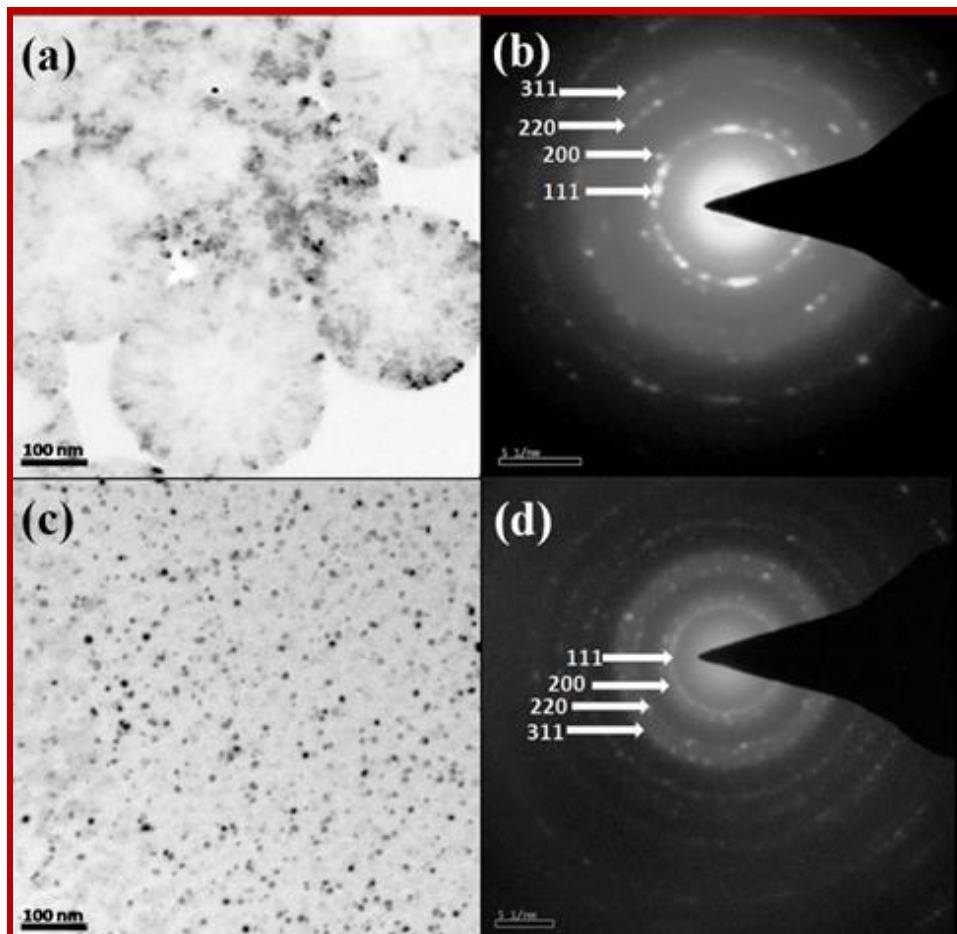

Figure 5.4 TEM images of the two CuNPs sols samples: B1 (a), B2 (c), and their corresponding electron diffraction patterns: B1 (b), B2 (d), respectively.

Figure 5.4 (b) and 5.4 (d) display the electron diffraction patterns of CuNPs samples B1 and B2 respectively. Indices of first four rings are indicated in Figures 5.4 (b) and 5.4

(d). The ring patterns of the samples could be indexed to FCC copper. This eliminates the possibility of oxidation of CuNPs within the limit of investigation.

Figure 5.5 shows the LSPR absorbance behaviour of the prepared CuNPs aqueous dispersions. Sample B1 displays a broadened featureless absorbance at about ~ 500 nm indicating the presence of very small separated Cu nanoparticles embedded in the polymer matrix. The LSPR absorbance spectrum of the sample B2 on the other hand shows a prominent maximum at ~ 593 nm which compares well with the characteristic plasmon absorption band of CuNPs.
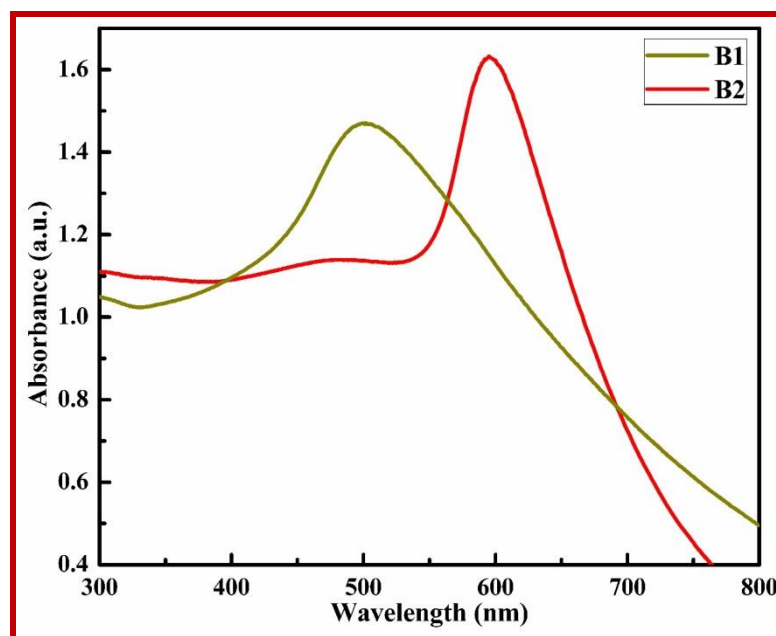
Figure 5.5 The UV–Vis absorption spectra of B1 and B2 CuNPs obtained by varying the amounts of AHH.

For the preparation of both CuNPs samples the amount of AHH added was in excess of the stoichiometrically required amount. That is, amount of excess AHH used to obtain B1 CuNPs is significantly different from that added to prepare B2 CuNPs. Hence, after synthesis, as compared to the B2 aqueous dispersion, less of undecomposed (or

excess) hydrazine hydrate is present in B1 dispersion. We believe that different amounts of excess AHH changes the dielectric environment and this may be the reason for the LSPR change observed.

The two stable stages (orange and reddish brown) were obtained in the same sol preparation with gradual increase in amount of AHH added. Therefore, the nanoparticles formed at the initial (yellow) stage were also there in the penultimate (reddish brown) stage and we may conclude that the average particle size became finer with increase in AHH addition. This could be explained by two possible mechanisms which may both be happening. One possibility is that the initial CuNPs formed at the first stage were some kind of aggregates of finer particles which broke into constituent particles on further addition of AHH. This may be due to heterogeneous nucleation density concentrated in a region with limited volume available for growth. The other alternative is that the nucleation rate increased with AHH addition (promoting homogeneous nucleation) resulting in finer nanoparticle sizes. To the best of our knowledge such separation of CuNPs growth stages has not been reported in earlier investigations following HH reductant addition to alkaline copper salt solution protocol.

5.3.2 Catalytic study

### 5.3.2.1 Catalytic Nip reduction with NaBH$_4$ and Gly

The progress with time of Nip reduction by NaBH$_4$ in presence of CuNPs catalyst, was tracked by decrease in intensity of absorption peak at ~ 401 nm. This is shown in Figure 5.6 (a). Simultaneously, a smaller absorbance maximum gradually increased at ~ 300 nm. This was due to the formation of the reaction product AP. Also, the spectrum

shows two isosbestic points at ~ 280 and ~ 316 nm which indicates that Nip was fully converted to AP without any side reaction [Kaur *et al*. (2016)].
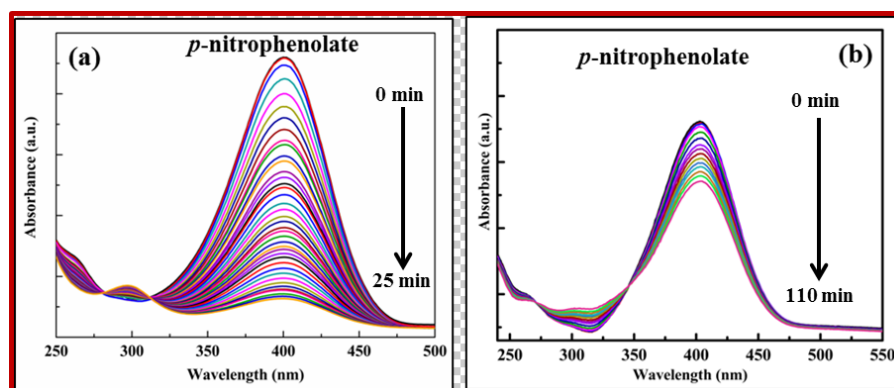
Figure 5.6 Variation in absorbance maximum of *p*-nitrophenolate (~ 401 nm) with NaBH$_4$ (a) and absorbance maximum of *p*-nitrophenolate (~ 406 nm) with glycerol (b) as reductant in presence of B2 CuNPs catalyst.

Figure 5.6 (b) shows the time evolution of the UV-visible spectrum, when Nip was reduced by Gly in presence of B2 CuNPs catalyst. The absorbance maximum of *p*-nitrophenolate at ~ 406 nm is seen to decrease with time. Concurrently, the absorbance at ~ 303 nm increases due to formation of AP. Since the isosbestic points are not very clear, therefore, a preliminary qualitative analysis and then ^{1}HNMR were carried out to identify the product formed. First azo dye test was performed to identify the presence of aromatic amine functional group in the product [Vogel (1978)]. This test results in the formation of orange coloured azo dye indicating the formation of *p*-aminophenol. Next, ^{1}HNMR spectrum of the product (Figure 5.7) was measured in DMSO as solvent. The NMR peaks observed are δ 8.35 (s, 2 H), 7.27 – 5.02 (m, 4 H), 4.38 (s, 2 H) which are corresponding to three types of H present in AP. This is akin to those presented in section 4.3.1.
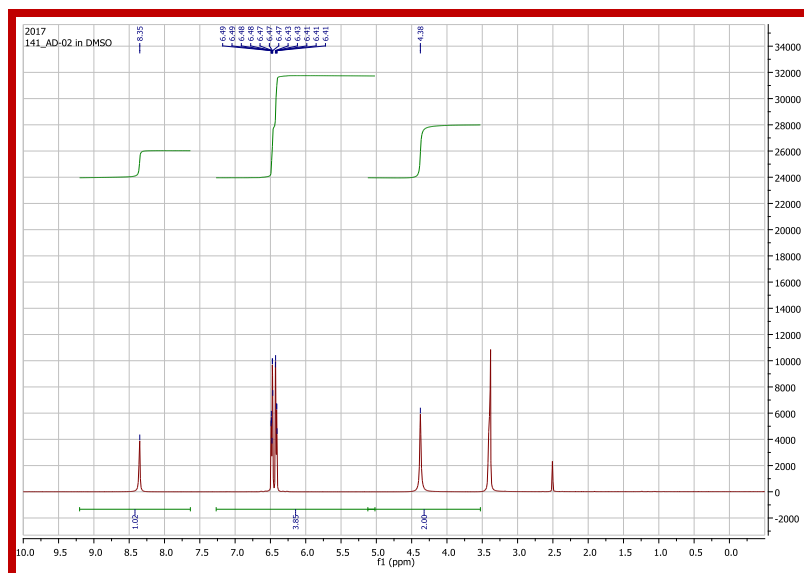
Figure 5.7 ^{1}HNMR spectrum of product of Nip reduction with glycerol in presence of B2 CuNPs.

Reduction kinetics

The slope of the linear fit of the plot between $\ln(-\frac{\partial A}{\partial t})$ versus $\ln(A)$ [from Eqn. 3.3] gives the order n with respect to reactant Nip [Alla *et al.* (2016), Gu *et al.* (2014)]. The amount of reducing agent $NaBH_4$ taken is almost ~ 40 times to that of Nip concentration, which is in large excess, therefore the concentrations of reductant remains almost constant during the reaction. The value of n is found to be 1. Hence, the reduction follows pseudo first order kinetics. In keeping with this result, $\ln(A/A_0)$ was plotted against time (Figure 5.8 (a)). This plot shows that initially there was a time gap (the induction time t_{ind}) during which no reduction took place. Thereafter, a nice linear fit to the plot, in accordance with pseudo first-order kinetics, was obtained (Figure 5.8 (a)). The apparent rate constant (k_{app}) was determined from the slope of the linear fit of $\ln(A/A_0)$ with time (after excluding t_{ind}). It can also be observed in Figure 5.8 (a), that the k_{app} of the reduction catalyzed by B1 CuNPs is lesser than the k_{app} obtained using B2 CuNPs.
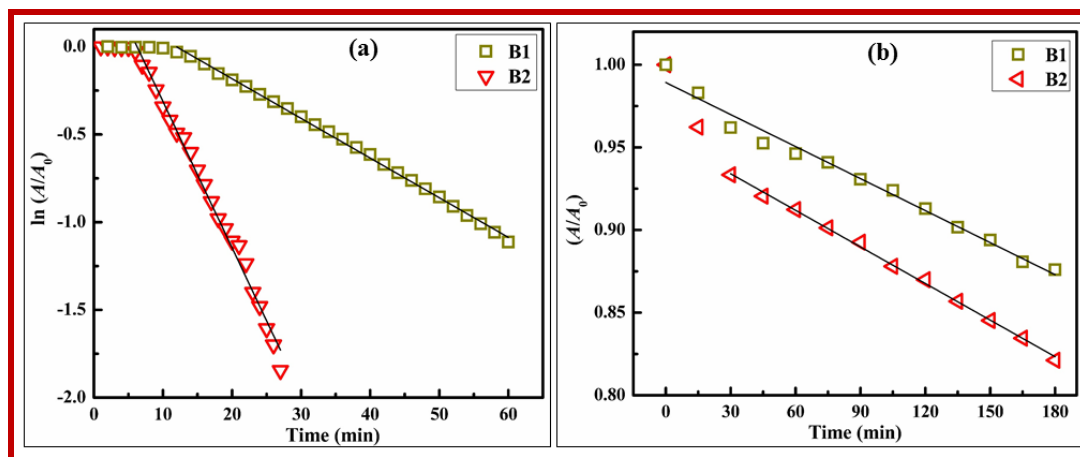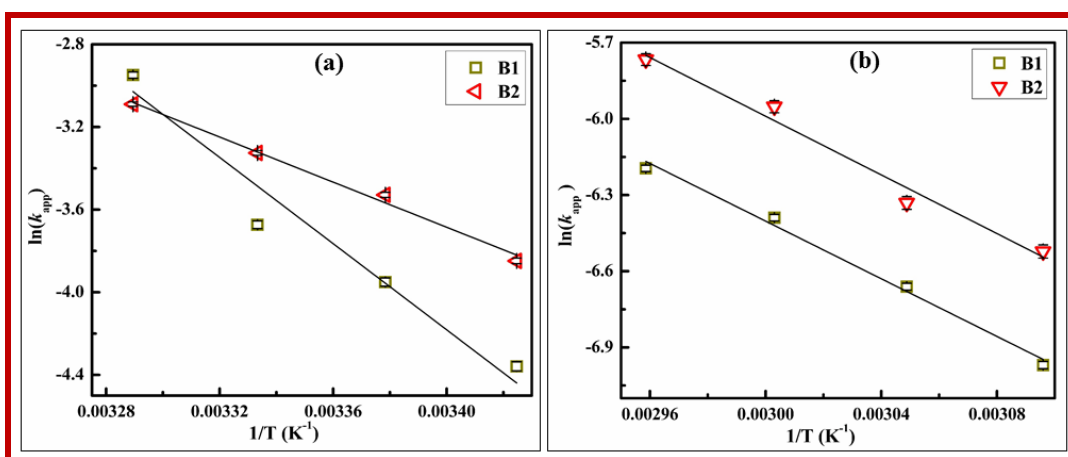
Figure 5.8 Variation of $\ln(A/A_0)$ [absorbance (A) measured at ~ 401 nm] Vs time with NaBH$_4$ reductant **8 (a)**. Variation of A/A_0 [absorbance (A) measured at ~ 406 nm] Vs time with Gly as reductant in presence of both CuNPs catalyst **8 (b)**. The R^2 value of all the fittings is ~0.98.

The order of reaction when Nip reduction is carried out with Gly in presence of CuNPs is found to be 0 [Eqn. 3.3]. This indicates that the Nip reduction with Gly in presence of CuNPs follows zero order kinetics. The order of reaction is found to be different from the (Nip) orders found for AgNPs catalysed Nip reduction with Gly mentioned in previous chapters. Good linear fits of A/A_0 versus time (for B1 and B2 CuNPs catalyzed Nip reduction with Gly) plots obtained (Figure 5.8 (b)). The k_{app} values were determined from the slopes of the linear fit of (A/A_0) against time and are tabulated in Table 5.1. The k_{app} value for B2 CuNPs is higher than that of B1 sample. This follows same trend to that of Nip reduction with NaBH$_4$.

Table 5.1 Average particle size, apparent reaction rate constants and activation energy for Nip reduction with NaBH$_4$ and Gly as reducing agent in presence of both B1 and B2 CuNPs catalyst.

Catalyst	Particle size d (nm)	Apparent reaction rate constant (k_{app}) NaBH$_4$ (min^{-1})	Apparent reaction rate constant (k_{app}) Gly (mol lit^{-1}min^{-1})	Activation energy (E_a) (kJ/mol) NaBH$_4$	Activation energy (E_a) (kJ/mol) Gly
B1	~ 11	0.0493	0.00058	~ 82.9	~ 47.2
B2	~ 9	0.263	0.00074	~ 45.7	~ 48.0

Figure 5.9 Arrhenius plot for Nip reduction reaction catalyzed by B1 and B2 CuNPs samples with reducing agents NaBH$_4$ (a) and Gly (b). Error bars are very small in most of the cases. The R^2 value of all the fittings is ~0.98.

One of the factors affecting the catalytic activity could be the size difference between the two CuNPs synthesized in the present study. Finer particle size would mean higher surface area or more number of surface catalytic active sites. However, the size difference between B1 and B2 CuNPs is relatively small, which cannot justify such a large difference in catalytic activity. Alternatively, higher catalytic activity of B2 (compared to B1) could be because of associated inherently different activation energies.

The $\ln(k_{app})$ versus 1/T plots for finding the activation energies are given in Figure 5.9. The values of activation energies, when the reduction is carried out by $NaBH_4$ and when it is done by Gly, are tabulated in Table 5.1. The activation energy of sample B2 (Table 5.1) was found to be nearly half of the value obtained for B1 nanoparticles. Therefore, it appears that the much higher catalytic activity obtained for B2 CuNPs was predominantly owing to its significantly lower activation energy. However, the activation energies associated with Nip reduction with Gly are almost similar.

Table 5.2 Comparison of turnover frequencies (TOF) for *p*-nitrophenol reduction by $NaBH_4$ in presence of CuNPs catalyst.

Sr. No.	Catalyst	Turnover Frequency (TOF) (min^{-1})	Reference
1	CuNPs	~ 0.01	[Deka *et al*. (2014)]
2	Cu Cubes	~ 136	[Zhang *et al*. (2013)]
3	SiNWAs–cu	~ 220	[Yang *et al*. (2014)]
4	B1 CuNPs	~ 356	This study
5	B2 CuNPs	~ 671	This study

Table 5.2 compares the TOF values for Nip reduction by $NaBH_4$ catalysed by different types of CuNPs reported in literature. It can be seen that the TOF values obtained for CuNPs prepared in the present study are definitely better than those reported earlier. Since, CuNPs have not been used as catalyst previously for reduction of Nip by Gly, therefore, such a comparison table cannot be given for this case.

5.3.2.2 Photocatalytic study

The order of reaction in photocatalytic Nip reduction with Gly also follows zero order kinetics (Figure 5.10). As both thermal and photocatalytic Nip reduction follows zero

order kinetics, this suggests that the mechanisms followed in the visible light photocatalytic

Nip reduction with Gly are similar.
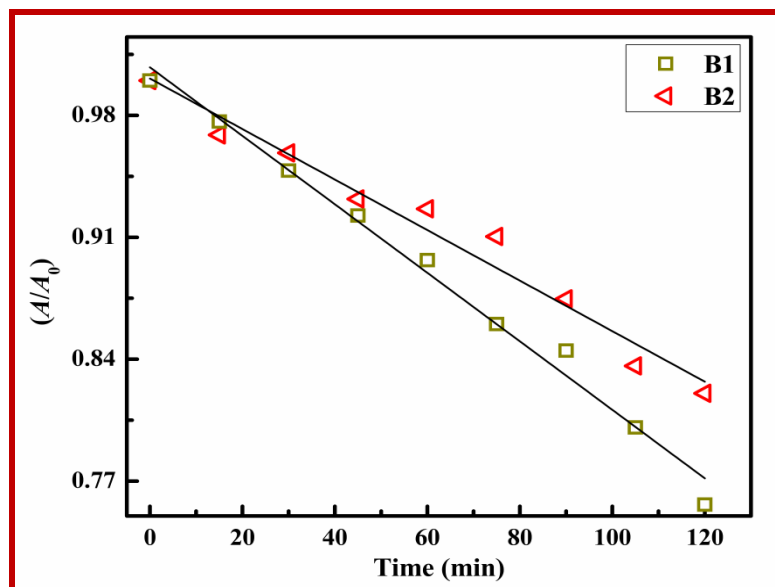
Figure 5.10 Variation of A/A_0 [absorbance (A) measured at ~ 406 nm] Vs time in photocatalytic Nip reduction with Gly. The R^2 value of all the fittings is ~ 0.98.

As this photocatalytic Nip reduction follows zero order kinetics, therefore, the k_{app}

values are obtained from the slope of the linear fit of A/A_0 versus time plot. The k_{app} values

of photocatalytic Nip reduction with Gly are tabulated in column 2 of Table 5.3. This

shows that B1 CuNPs has higher photocatalytic k_{app} compared to B2. For better comparison

of catalytic activity of these catalysts, the PTOF are calculated with the help of Eqn. 3.5

and the values obtained are tabulated in Table 5.3.

The PTOF values also show the same trend as the photocatalytic k_{app}. The TOF

values of CuNPs catalyzed Nip reduction with Gly without light at the same temperature

(306 K) are given in the same Table 5.3 for comparing the effect of visible light in

photocatalytic Nip reduction in presence of plasmonic CuNPs. Table 5.3 shows that the

catalytic activity in absence of light and photocatalytic activities follow opposite trends.

The reason for this appears to be the different wavelengths at which maximum LSPR absorbance is observed for B1 and B2. While B1 shows LSPR maximum at ~ 500 nm, the value for B2 is ~ 593 nm.

Table 5.3 Displays the photocatalytic apparent reaction rate constant, Thermal (TOF) and photocatalytic turnover frequency (PTOF) for Nip reduction with Gly as reducing agent at 306 K.

Catalyst	Photocatalytic apparent reaction rate constant (k_{app}) (mol lit^{-1} min^{-1})	Turn over frequency (min^{-1})	
		TOF	PTOF
B1	0.00197	~ 2.5	~ 6.0
B2	0.00145	~ 3.5	~ 4.5

It can be seen that the LSPR maximum of B1 is nearer to the absorbance of Nip. Following the mechanism proposed in Chapter-3 and 4, it appears that plasmonic excitation of electrons is better when the LSPR absorbance is around ~ 500 nm. On the other hand, the wavelength of the re-emitted light may also be more suited to excite Nip adsorbed on the catalyst surface.

5.3.2.3 Methyl orange oxidation thermal and photocatalytic

Figure 5.11 shows the UV-visible spectrum of MO degradation when the reaction is carried out in presence of B2 CuNPs. All three peaks present initially in the UV-visible spectrum of MO in acidic medium undergo degradation together with progress of time.
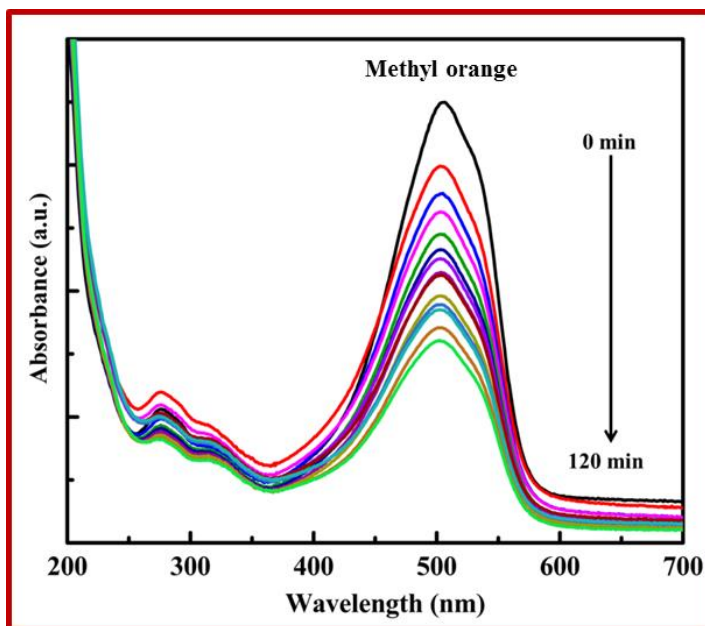
Figure 5.11 Variation of absorbance maximum of MO (~ 506 nm) with H_2O_2 oxidizing agent in presence of catalyst B2 CuNPs catalyst.

Moreover, there is no sign of any new absorption in these regions. This suggests that MO degradation definitely occurs till stage (E, F, G) of the well-known mechanism proposed in in Chapter-3 (Figure 3.16).

The order of MO degradation is obtained from the slope of the linear fit of plot between $\ln\left(-\frac{\partial A}{\partial t}\right)$ versus $\ln(A)$ [Eqn. 3.3]. The orders, thus calculated, are 2 and 0 for thermally and photocatalytically catalyzed MO degradations respectively. Consequently, the respective k_{app} values are found from the slopes of the linear fits for the plots between $1/A_t$ versus time for thermal and A/A_0 versus time for photocatalytic MO degradations (Figure 5.12). Table 5.4 summarizes the thermal and photocatalytic apparent reaction rate constants associated with oxidative MO degradation in presence of CuNPs catalyst. Further, this degradation was studied at different temperatures to calculate the activation energies by utilizing the Arrhenius equation given in Chapter-3 [Eqn. 3.4]. The linear plots

between $\ln(k_{app})$ and 1/T is shown in Figure 5.13. The activation energy in presence of B1

and B2 CuNPs are also mentioned in Table 5.4.
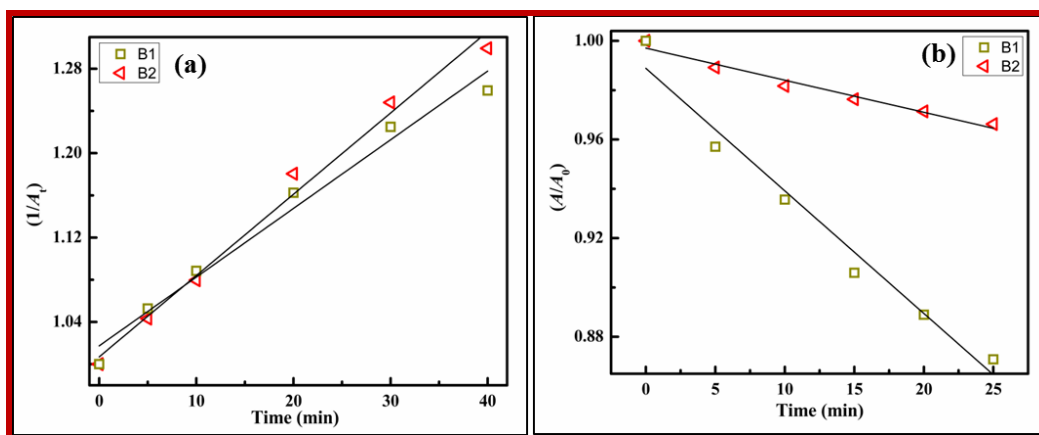
Figure 5.12 Variation of $1/A_t$ [absorbance (A) measured at ~ 506 nm] versus time for thermal (a) and photocatalytic (b) MO degradation in presence of B1 and B2 CuNPs catalyst. The R^2 value of all the fittings is ~ 0.97.
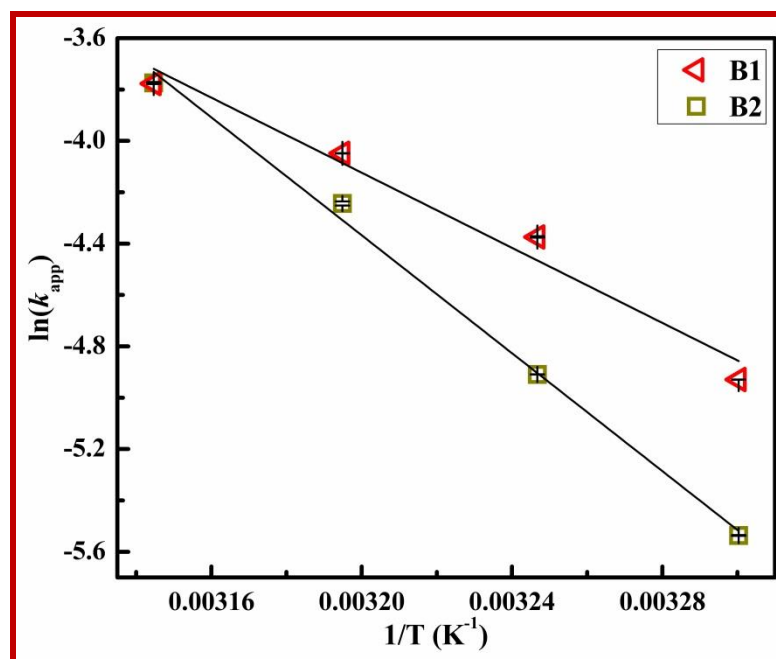
Figure 5.13 Arrhenius plot for MO degradation catalyzed by B1 and B2 CuNPs samples. Error bars are very small in most cases. The R^2 value of all the fittings is ~ 0.98.

In the thermally catalyzed MO oxidation reaction, catalyst B1 exhibits lesser activity than B2. In both $NaBH_4$ and Gly reduction of Nip (in absence of light) also the activity exhibited by B2 is more. However, the activation energy for the MO degradation reaction catalyzed by B1 is lesser. Although, the size difference is not much but it seems that B2 offers more surface area and hence active sites for MO degradation. Overall, the catalytic activity for MO degradation is lesser in comparison to AgNPs investigated in Chapters-3 and 4.

Table 5.4 Apparent reaction rate constant and turnover frequency for thermal (TOF) and photocatalytic (TOF) MO degradation at 306 K in presence of both CuNPs catalyst. Activation energy for thermal oxidative MO degradation is also mentioned in this table

Catalyst	Apparent reaction rate (k_{app})		Activation energy	Turn over frequency (min^{-1})	
	Thermal (mol^{-1} lit min^{-1})	Photo (mol lit^{-1} min^{-1})	(E_a) (kJ/mol)	Thermal	Photo
B1	0.0065	0.0013	~ 61.2	~ 0.5	~ 1.5
B2	0.0077	0.0047	~ 95.3	~ 1.2	~ 1.7

On the other hand, the trend is reversed in case of photocatalytic degradation of MO. That is, the activity exhibited by B1 is more than that found for B2. It can be seen that the LSPR maximum of B1 is similar to the absorbance of MO. Apparently, the plasmonic excitation of electrons is better when the LSPR absorbance is around ~ 500 nm. Following the mechanism given in Chapter-3, it is possible that the electrons excited in this manner are transferred to reduce H_2O_2 leading to the formation of hydroxyl radicals.

5.4 Conclusions

The controlled addition of AHH (reductant) in presence of PVP to the copper salt solution resulted in two stable aqueous sols of CuNPs with different average sizes (~ 9 and ~ 11 nm). This may be due to lesser nucleation rate for smaller AHH addition and further increase in nucleation rate on excess AHH addition. These CuNPs exhibit widely different LSPR absorbance values. The synthesized CuNPs were then utilized as catalysts for reduction of Nip to AP with $NaBH_4$ or Gly as the reducing agent. Catalytic activities of the PVP stabilized CuNPs prepared in the present study for Nip reduction by $NaBH_4$, were found to be significantly higher than other CuNPs reported earlier in literature. Prepared CuNPs were also found to catalyze Nip reduction by Gly and Fenton like MO oxidative degradation. On carrying out these reactions under visible light, significant enhancement in photocatalytic activity was observed. However, the CuNPs with LSPR absorbance around ~ 500 nm were found to more active photocatalytically. It seems that plasmonic excitation of electrons required for their direct injection into adsorbate LUMO orbitals, is more efficient when LSPR absorbance is at ~ 500 nm.